Research Square

Preprints are preliminary reports that have not undergone peer review.
They should not be considered conclusive, used to inform clinical practice,
or referenced by the media as validated information.

Quantitative evaluation of single-grating phase-contrast imaging with a femtosecond laser–plasma Kα X-ray source

Georges Giakoumakis
georges.giakoumakis@onera.fr
Office National d'Études et de Recherches Aérospatiales
Amélie Ferré
Lasers, Plasmas et Procédés Photoniques
Daria Gudz
Lasers, Plasmas et Procédés Photoniques
Mouad Saliji
Office National d'Études et de Recherches Aérospatiales
Jérôme Primot
Office National d'Études et de Recherches Aérospatiales
Olivier Utéza
Lasers, Plasmas et Procédés Photoniques
Raphaël Clady
Lasers, Plasmas et Procédés Photoniques
Adrien Stolidi
CEA, List

Article

Keywords:

Posted Date: August 11th, 2026

DOI: https://doi.org/10.21203/rs.3.rs-10535729/v1

License: This work is licensed under a Creative Commons Attribution 4.0 International License.
Read Full License

Additional Declarations: No competing interests reported.

Version of Record: A version of this preprint was published at Scientific Reports on November 22nd, 2026. See the published version at https://doi.org/10.1038/s41598-026-78588-x.

Quantitative evaluation of single-grating phase-contrast imaging with a femtosecond laser–plasma Kα X-ray source

Georges Giakoumakis[1,+,*], Amelie Ferré[2,+,*], Daria Gudz[2], Mouad Saliji[3,5], Jérôme Primot[4], Olivier Utéza[2], Raphaël Clady[2], and Adrien Stolidi[5]

[1]DMAS, ONERA, Université Paris-Saclay, Palaiseau, 91120, France
[2]Aix-Marseille Université, CNRS, LP3 UMR 7341, Marseille, 13288, France
[3]DPHY, ONERA, Université Paris-Saclay, Palaiseau, 91120, France
[4]DOTA, ONERA, Université Paris-Saclay, Palaiseau, 91120, France
[5]Université Paris-Saclay, CEA, List, Palaiseau, F-91120, France
[*]georges.giakoumakis@onera.fr and amelie.ferre@univ-amu.fr
[+]these authors contributed equally to this work

ABSTRACT

We present the first implementation of an X-ray phase-contrast imaging approach using single 2D-grating phase retrieval and a quasi-monochromatic hard Kα X-ray source generated *via* high-intensity femtosecond laser–plasma interaction. To highlight its pertinence, we demonstrate quantitative phase-contrast measurements of a known canonical physical object, retrieving its projected thickness with high-fidelity, under varying experimental conditions. As a marker of such performance, an average correlation mean score up to 0.92 is obtained between simulated and experimental phase images. The consistency of the retrieved phase gradients is further quantitatively evaluated using the Confidence Map, a self-consistency metric derived directly from the acquired data. This framework supports a systematic parametric study aimed at quantifying the influence of X-ray source characteristics on phase retrieval and thus optimizing imaging performance by balancing exposure time and spatial resolution. Two operating regimes are investigated: X-ray iso-flux conditions with varying spatial coherence of the X-ray source and iso-acquisition-time conditions with varying X-ray photon flux. This work establishes a pathway toward minimizing exposure times while preserving accurate phase retrieval, with the long-term objective of enabling short-time exposure of time-resolved phase-contrast imaging.

Introduction

X-ray phase contrast imaging (XPCI) has emerged as an effective imaging modality for investigating weakly absorbing materials, such as biological soft tissues, polymers, or composite materials. Unlike conventional X-ray absorption imaging, XPCI relies on the detection of X-ray phase shifts induced by the sample to generate image contrast, rather than from X-ray attenuation. Since these phase shifts are governed by the real part of the complex refractive index $n = 1 - \delta + i\beta$, XPCI provides a direct access to the decrement δ, which is typically several orders of magnitude larger than the absorption term β for weakly absorbing materials[1]. This is particularly advantageous for discriminating objet constitutents with low atomic number or low density, for which conventional absorption contrast is poor. Today, XPCI finds applications in fields such as medicine[1], biology[2,3], and materials science[4–6], enabling computed tomographic reconstructions[7] and dynamic imaging[5]. It has also been proposed as a promising diagnostic tool for the study of Warm Dense Matter, laboratory astrophysics, and inertial confinement fusion[8]. X-ray phase contrast imaging techniques can be broadly classified into two main categories[9]. The first relies on free-space propagation, where the object itself generates the measurable intensity modulation[10,11]. The second introduces an additional modulating element, such as a regular grid[12,13], masks[14], gratings[15], or a random modulator[16], to encode the phase signal into intensity variations. Initially developed using high-brightness pulsed sources such as synchrotrons[17], these methods have since been adapted for continuous sources, such as X-ray tubes. Alternatively, pushing the applicability of XPCI technique with the laser–plasma-based X-ray sources technology[18–20] is of valuable interest as it opens access to the measurement of rapid dynamics to the widest audience, complementary to large-scale XFEL/synchrotrons installations, or to X-ray tube technologies. Among them, laser-driven Kα X-ray sources are generated by focusing an intense femtosecond laser onto a high-Z solid target, producing a repeatable short-pulse X-ray flux with a well-defined X-ray emission volume. Their emission spectrum consists of a broad Bremsstrahlung background superimposed by large-amplitude monochromatic Kα and Kβ lines[21], characteristic of

the target material. Interestingly, demonstration of such X-ray sources with Kα X-ray flux in excess of 10^9 ph/shot has been done at high-repetition rate ($\geq$ 1 kHz)[22]. These femtosecond X-ray sources are temporally incoherent and divergent but have adjustable spatial coherence. Free-space propagation was the first XPCI modality demonstrated with laser-based Kα X-ray sources, initially on biological samples[23]. This approach is straightforward, as it does not require any optical elements between the source and detector. Phase contrast arises from Fresnel diffraction induced by the sample during free-space propagation. However, sufficiently long propagation distances are generally required to generate measurable intensity modulations, detected as intensity overshoots. More, quantitative phase retrieval from propagation-based images remains a challenging inverse problem. Classical retrieval algorithms generally rely on prior assumptions regarding the sample composition, the δ/β ratio or the source spectrum[11,24]. Nevertheless, recent model-based, iterative and physics-informed approaches have substantially relaxed, or in some cases eliminated, several of these assumptions[25,26]. Alternatively to free-space propagation, quantitative phase information can be obtained using phase-gradient imaging techniques, which rely on direct measurements of the wavefront deflection instead of Fresnel diffraction by adding a modulating element. For instance, intensity modulation techniques such as Talbot-Lau interferometer have been demonstrated to laser-induced Kα X-ray sources[27]. The first X-ray grating, an absorption grating, decomposes the incoherent X-ray source into multiple independent higher spatially coherent beamlets. A second-stage phase grating modulates the incident X-ray beam intensity, thereby creating a reference pattern –called interferogram– which is captured when the transmitted X-ray beam is deflected toward a final-stage absorption grating (analyzer grating). Phase variations induced by adding the sample are then encoded in one spatial direction with higher sensitivity, by modifying the interferogram and simplifying the retrieval of the phase image. With a one-dimensional grating, obtaining two-dimensional phase information typically requires two separate acquisitions, one for each transverse direction. Achieving high fringe intensity contrast relies on precise alignment and excellent mechanical stability of the optical arrangement[28]. In addition, restrictive locations of gratings are required to match the benefit of the periodic nature of Talbot effect and to correctly sample the pattern by the analyser. Due to absorption, only 11% of the incident X-ray flux passing through the interferometer has been used for this experiment[27]. Although effective, this multi-grating approach demands high X-ray flux, long acquisition times, and higher target consumption, resulting in significant technological cost. These constraints highlight the need for alternative imaging protocols that may propose better performance and more efficient trade-offs. We present, in this manuscript, the first implementation of a multi-lateral shearing interferometry[29,30] (MLSI) XPCI technique with a TW-class Ti:Sapphire laser driver and a Mo (17.48 keV) massive target[31] at a repetition rate of 100 Hz. Our approach combines a pulsed laser-driven Kα X-ray source, a single low-attenuation checkerboard grating, and a high-spatial-resolution detector into a simple and compact architecture for phase-sensitive X-ray imaging. This specific achromatic imaging approach simultaneously measures the X-ray wavefront phase shift induced by the sample along multiple orientations.

To demonstrate the potential of this approach, we present in this paper a systematic parametric study of MLSI using laser–plasma Kα X-ray sources operated under different laser–target interaction regimes. To this end, the parametric investigation strategy and the experimental setup are first presented. The influence of the laser–plasma Kα X-ray source parameters on MLSI phase retrieval is then investigated through two complementary experimental approaches: an iso-flux investigation and a fixed acquisition-time study. The respective influence of X-ray photon flux, source size, and acquisition time on phase retrieval is quantitatively assessed through complementary image quality metrics. Finally, results are discussed regarding image quality evaluation, and the implications for MLSI with laser-driven X-ray sources are addressed.

Experimental parametric investigation

The main objective of this study is to establish a controlled framework for quantifying the influence of X-ray source characteristics on MLSI performance, by distinguishing the respective contributions of photon statistics and source size to the quality of the retrieved phase images. The parametric study is therefore structured into two complementary experimental investigations:

- An iso-flux investigation, where the number of detected X-ray photons is kept constant by adjusting the acquisition time for different energies of the laser driver.
- A fixed acquisition-time investigation, where the detected X-ray photon flux varies with the laser energy.

The workflow is illustrated in Figure 1. In our previous studies[32,33], the X-ray source size and the generated X-ray photon flux exhibited an approximate power-law dependence on the laser intensity on target, with fitted exponents of $\alpha_{\text{size}} \approx 0.34$ and $\alpha_{\text{flux}} \approx 1.4$, respectively. These scaling laws reveal a limited laser intensity range in which both a sufficiently high photon flux and a small source size can be achieved simultaneously. Based on this analysis, two laser energies $\{E_1, E_2\}$ are selected for the present study to investigate complementary operating regimes. The 4 mJ configuration (E_2) has therefore been selected as a lower-energy operating point, providing a favorable compromise between source size limitation and photon statistics. Conversely, the 12 mJ configuration (E_1) has been chosen close to the onset of the source-size growth regime, where the increase in photon flux is significant while the X-ray source size is still compatible with high-resolution phase-contrast

imaging. In particular, the focal X-ray spot size S, characterized by its transverse dimensions $\{S_X, S_Y\}$, directly influences the geometrical blur $b = \{b_x, b_y\}$ according to the standard relation $b = (M-1) \times S$, where M refers to the magnification factor of any component placed into the optical path. Note that (X,Y) refer to the two spatial transverse coordinates in the X-ray target plane, while (x,y) rely to the two transverse spatial coordinates in the detector plane. When the geometrical blur becomes significant compared with the detector pixel size and the grating periodicity, the interference pattern is degraded, resulting in a loss of image resolution and contrast, thus compromising MLSI performance. The selected configurations therefore represent optimized operating conditions for MLSI, offering a good balance between photon efficiency and spatial resolution.

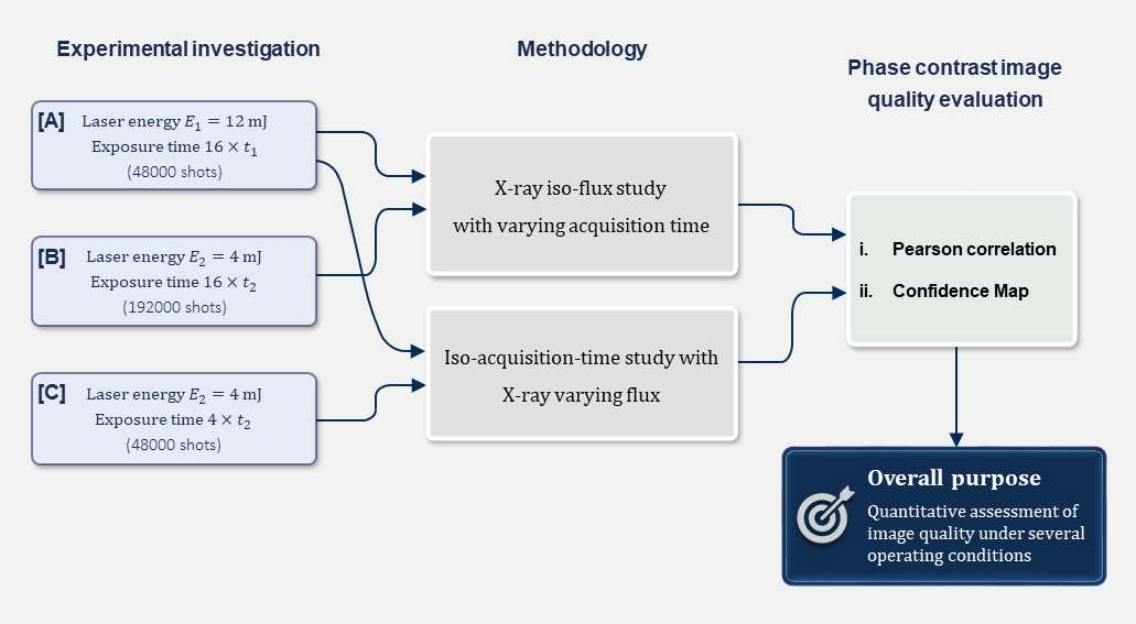

Figure 1. Overview of the experimental strategy adopted to evaluate phase image quality in MLSI using laser–plasma Kα X-ray source parameters: $E_1 = 12$ mJ ; $E_2 = 4$ mJ ; $t_1 = 30$ s ; $t_2 = 120$ s.

To quantitatively assess phase image quality, two complementary approaches are adopted: the first compares the retrieved phase image with the theoretical phase response of the sample, here a set of calibrated polymethyl methacrylate (PMMA) microspheres. Their well-defined geometry and composition enable accurate prediction of the expected phase signal under idealized imaging conditions, assuming a monochromatic X-ray beam and noise-free measurements. The corresponding simulated 2D reference phase image is given by: $\phi_{num}(x,y) = \frac{2\pi\delta}{\lambda} e_p(x,y)$ where λ is the wavelength of the chosen Kα emission line, $e_p(x,y) = \sqrt{R^2 - x^2 - y^2}$ is the projected thickness, with R the radius of each PMMA sphere, and δ refers to the refractive index decrement for PMMA, depending on the Kα emission line. An example of the simulated data is displayed in Figure 5 (g) (see the Methods section). The agreement between experimental and simulated phase images is therefore assessed quantitatively using a Pearson correlation estimation, assuming a linear correspondence between the two datasets. The second quantitative evaluation relies on a self-consistency approach, known as the Confidence Map, which evaluates phase measurement errors directly from the acquired data[34]. By leveraging MLSI's ability to simultaneously measure at least two orthogonal phase gradients, the curl of these gradients is performed. Under ideal conditions (continuous and twice-differentiable wavefront), this curl should be equal to zero at any point (x,y) of the image. However in practice, local deviations from zero arise from several sources of error, including measurement noise or errors originating from undersampling. The Confidence Map identifies, quantifies, and visualizes these contributions as colored pixels on the image. By using a statistical generalization based on generalized Gaussian distributions, each pixel is assigned to a family of errors (noise η_n in green pixel, medium-magnitude and high-magnitude undersampling η_u^M, η_u^H, respectively in cyan and red pixel), and the mean and standard deviation of the Confidence Map values serve as metrics for image quality[35]. A decrease in the mean value indicates an overall reduction in errors, while a decrease in the standard deviation reflects a more localized distribution of residual errors across the image. These quantitative evaluations are further supplemented by computing the fringe contrast-to-noise ratio (f-CNR) and the harmonic signal-to-noise ratio in the Fourier domain (h-SNR) of the raw data. Since phase retrieval in MLSI relies on the analysis of the interferogram, these indicators provide complementary information for interpreting any variations in phase image quality. The detailed calculation procedure is described in the Methods section.

Experimental setup

Figure 2 depicts the schematic layout of the MLSI-XPCI setup used for the parametric study presented in this work. The femtosecond high flux Kα source is operated at 17.48 keV at a repetition rate of 100 Hz. This chosen Kα emission line is well suited for achieving high phase contrast sensitivity in a wide range of materials due to a δ/β ratio close to 1000[1]. Previous studies conducted on the same Kα laser–plasma platform demonstrated its capability to generate X-rays suitable for phase-contrast imaging of weakly absorbing objects under free-space propagation conditions[31,32]. The PMMA microspheres are of radius of $R = 750$ µm with a low size dispersion ($\pm 2.5\%$ as certified by the supplier Goodfellow), and a refractive index decrement $\delta = 8.73\ 10^{-7}$ at 17.48 keV[36]. Aside from their well-defined geometry and studied composition allowing an accurate prediction of the theoretical phase signal, the motivation behind selecting such imaging object also lies in the ability to explore any anisotropy information arising from the imaging system, particularly the from the X-ray source spot. The experimental implementation of MLSI relies on a single 2D-checkerboard phase grating, designed by Microworks, with periodicity $a = 36$ µm along the two transverse directions. It consists of squared gold platforms of size $a/2$ and thickness of 1.7 µm (inducing a [0-$\pi/2$] phase shift at 17.48 keV) deposited on a polyimide substrate. Thanks to its low absorption, more than 85% of the Molybdenum Kα line (17.48 keV) is transmitted through the interferometer, preserving the X-ray flux. To avoid contamination from debris generated during Kα production, the grating is placed outside the interaction chamber immediately downstream of the beryllium exit window. This arrangement imposes a minimum source-to-grating distance. The experimental geometry, including the choice of working distances and the impact of the source polychromaticity on the MLSI interferogram, is detailed in the Methods section. For a polychromatic X-ray source, the spectral bandwidth $\Delta\lambda$ can affect the recorded interferogram depending on the propagation distance between the grating and the detector. Beyond the corresponding achromatic distance, the MLSI signal becomes essentially insensitive to the residual spectral bandwidth[30]. In the cone-beam geometry, this distance is $d_{\mathrm{ach,c}} = 20$ cm (see Methods). The selected detector position satisfies the condition $(d_{\mathrm{tot}} - d_{\mathrm{sg}}) > d_{\mathrm{ach,c}}$, ensuring that the residual spectral content of the Kα source does not introduce significant distortions in the measured interferogram.

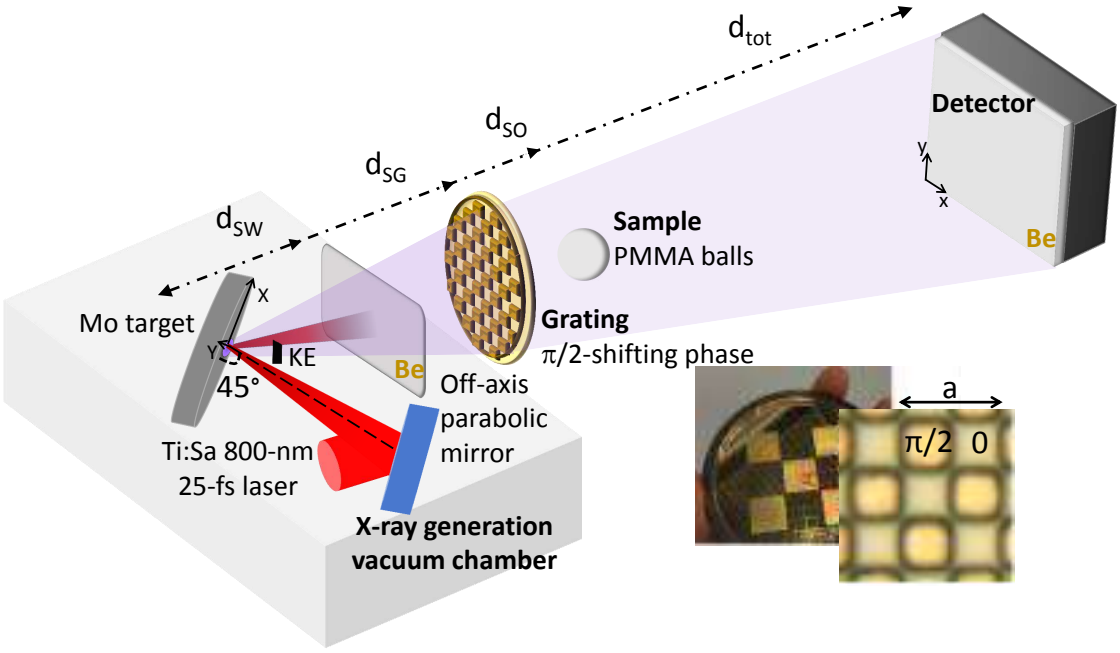

Figure 2. MLSI XPCI setup using pulsed Kα 17.48 keV source and a single 2D-grating. The transmitted X-rays through the Beryllium (Be) window propagate in air where the MLSI setup is mounted.The 2D grating produces a reference intensity pattern obtained without the sample. Spatial modulations of the reference intensity pattern induced by the sample are detected by a 16-bits direct detection PIXIS-XB: 1024BR camera from Princeton Instruments of a surface of 1024×1024 pixels array and a pixel size a_{pix} equal to 13 µm sideways. The characteristic distances are: $d_{sw} = 17$ cm, $d_{sg} = 22$ cm, $d_{so} = 25.5$ cm and $d_{tot} = 92$ cm.

As previously demonstrated[37], varying the laser driver intensity can shape the X-ray source flux and size. We achieve that by changing only the laser pulse energy, using a half-wave plate ($\lambda/2$) and a polarizer located in the final power amplifier of the laser chain, while keeping the laser spot size and pulse duration constant. Beforehand, the FWHM X-ray source dimensions have been determined using a knife-edge technique[38]. As previously reported, the measured source sizes are larger than the

laser focal spot and increase with laser intensity[21,39,40]. The emitted Kα line photon flux is calculated from the reconstructed spectrum. The X-rays are detected over a spectral bandwidth of around 25 keV with a prominent Kα peak at 17.48 keV (see details in Methods). Finally, phase retrieval in MLSI is based on the comparison between the reference interferogram, recorded without the sample, and the sample interferogram acquired under identical conditions. The presence of the sample locally distorts the periodic fringe intensity pattern through phase shifts introduced by the object. Since the interferogram is periodic along several orientations, the fringe deformations are first analyzed in the Fourier domain to extract two orthogonal phase gradients images. The quantitative phase image is then reconstructed by integrating both gradient components. The complete phase retrieval procedure and processing workflow are described in the Methods section. The X-ray source characteristics used in this study are summarized below in Table 1.

Laser energy (mJ)	Laser intensity (W cm^{-2})	S_X (µm)	S_Y (µm)	Kα photon flux (sr^{-1} s^{-1})	Kα photons (%)
12	1.2×10^{18}	27	23	3.2×10^{9}	27
4	4.0×10^{17}	16	13	8.0×10^{8}	20

Table 1. Parameters of the laser–plasma X-ray source used for the parametric study, as a function of the laser experimental conditions.

Iso-flux experimental investigation with variable acquisition time and laser driver energy

In this first investigation, the total amount of incident photons is kept constant while varying the laser driver energy. Since the X-ray photon flux at the laser energy E_2 is four times lower than at E_1 (see Table 1), the corresponding images are acquired with an exposure time increased by the same factor ($t_2 = 4 \times t_1$). This approach ensures that the photon noise level remains similar across all acquisitions, allowing an isolated evaluation of the effect of the X-ray source size on the phase image quality.

Figure 3 (a) and (d) present the raw interferograms acquired with a set of four PMMA microspheres arranged identically for each operating conditions. Based on an initial raw data analysis, a strong relationship between the fringe intensity contrast and the laser energy is observed in the interferograms. The fringe contrast-to-noise ratio (f-CNR) rises from 2.02 for laser energy E_1 with exposure time t_1 (configuration $[A]$), to 3.98 for laser energy E_2 with exposure time t_2 (configuration $[B]$). This behavior is also reflected in the harmonic signal-to-noise ratio, particularly in the case of the harmonics of interest $H_{-1,1}$ and $H_{1,1}$ exploited to perform phase retrieval. In this case, h-SNR$_{E_1,t_1}(H_{-1,1},H_{1,1}) = (13.69,\ 13.68)$, and h-SNR$_{E_2,t_2}$ $(H_{-1,1},H_{1,1}) = (20.71,\ 20.50)$. The improvement in f-CNR and h-SNR values can be attributed to the decrease of the X-ray source size at lower laser energy, which reduces the geometrical blur and preserves the high-frequency harmonic components of the interferogram, carrying the phase information.

The corresponding retrieved phase images are displayed in Figure 3 (b) and (e). Quantitative assessment of the phase image quality is first established by Pearson correlation. For configuration $[A]$, the correlation mean scores along the x and y axis are $\rho_x = 0.809$ and $\rho_y = 0.806$ respectively, whereas they reach $\rho_x = 0.88$ and $\rho_y = 0.92$ for configuration $[B]$ (see Table 2). The higher global correlation obtained at 4 mJ therefore confirms a better agreement between the retrieved and theoretical phase images at the lowest laser energy. Moreover, the Confidence Maps are computed for each dataset (see Figure 3 (c) and (f)). Noise alerts η_n (green) and undersampling alerts η_u^M and η_u^H (cyan and red, respectively) are displayed using the same dynamic scale, ensuring a consistent representation of error amplitudes across both operating conditions. Compared with the configuration $[A]$, the configuration $[B]$ exhibits a significant reduction in the amplitude of both the noise alerts η_n suggesting that the noise influence has been significantly attenuated through phase extraction. A similar reduction is qualitatively observed in the displayed Confidence Maps for the medium-amplitude undersampling alerts η_u^M, while the high-amplitude undersampling alerts η_u^H (red) are removed within the PMMA microspheres (see Figure 3 (f)). The remaining η_u^H alerts are mainly confined to the image boundaries, where they reveal residual phase retrieval artefacts. The mean amplitudes (μ) and corresponding standard deviations (σ) of the Confidence Map alerts are summarized in Table 2 for each operating condition. These results are consistent with the Pearson correlation analysis.

Lastly, at 4 mJ, the significantly lower horizontal Pearson correlation score (ρ_x) compared with its vertical counterpart (ρ_y) reveals a directional degradation of the retrieved phase image. This behavior is consistent with the anisotropic spatial coherence of the X-ray source, which is lower along the horizontal direction owing to the larger effective source size (S_X). At 12 mJ, no statistically significant difference is observed between the two directions, with ($\rho_x = 0.809$) and ($\rho_y = 0.806$). Under the present experimental conditions, photon noise is expected to dominate the phase-image uncertainty at this energy and to affect both directions approximately isotropically. This isotropic contribution may therefore mask the directional signature associated with the source anisotropy, preventing a reliable quantification of its effect on the reconstructed phase image.

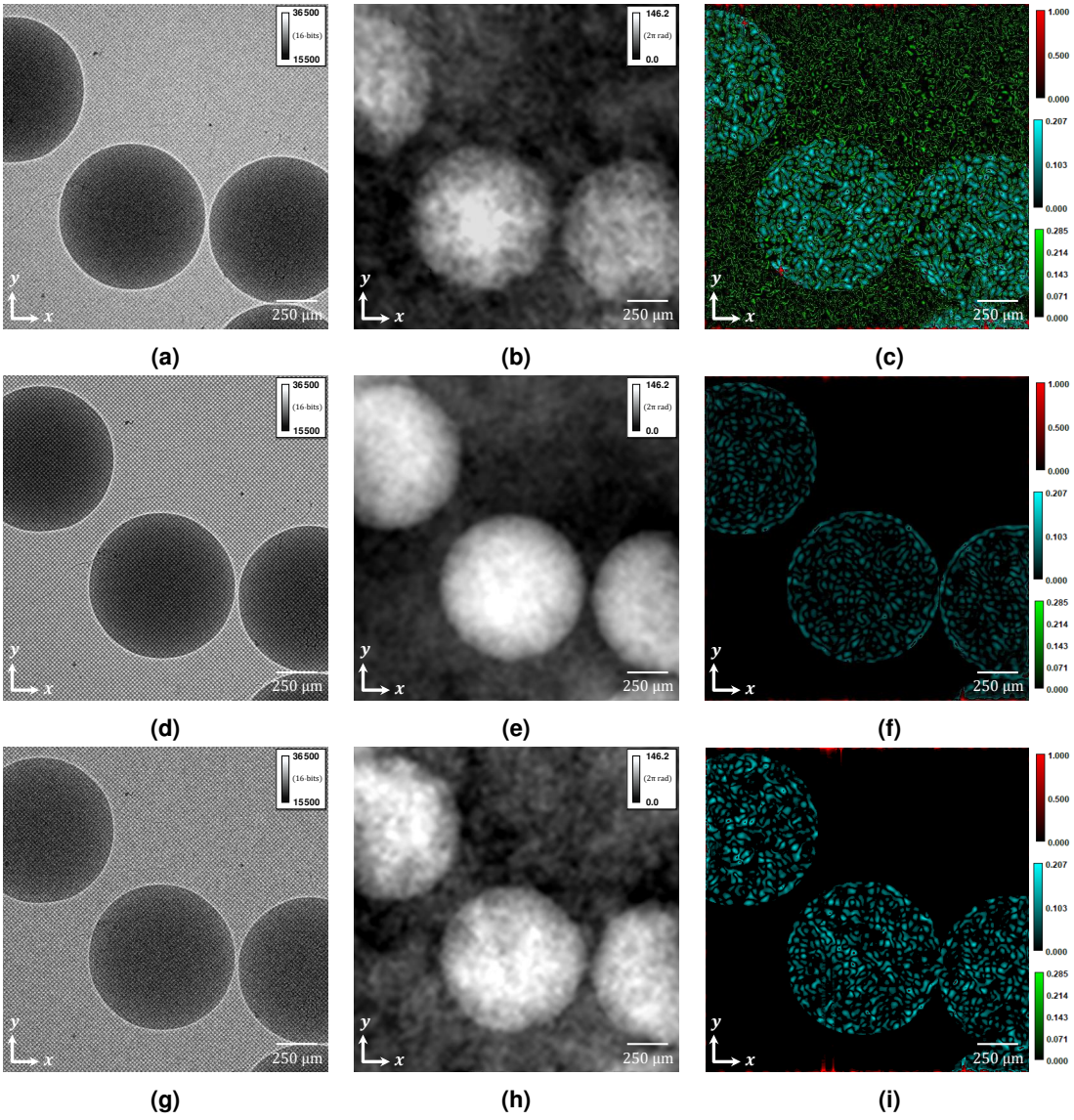

Figure 3. Top row: (a) raw interferogram obtained at laser energy E_1 with integration time t_1 averaged 16 times (configuration $[A]$); (b) associated phase image and (c) Confidence Map. Middle row: (d) raw interferogram obtained at laser energy E_2 with integration time t_2 averaged 16 times (configuration $[B]$); (e) associated phase image and (f) Confidence Map. Bottom row: (g) raw interferogram obtained at laser energy E_2 with integration time t_2 averaged 4 times (configuration $[C]$); (h) associated phase image and (i) Confidence Map.

Fixed acquisition-time study with variable X-ray flux and laser driver energy

The second experimental study explores two imaging configurations acquired with different X-ray flux while maintaining the same total acquisition time. This investigation enables the net impact of laser energy on phase image quality to be assessed under realistic acquisition constraints, where photon statistics and source size evolve simultaneously. It reflects the practical operating conditions of laser-driven XPCI systems, in which the total acquisition time is often constrained by the application and cannot be increased to compensate for a lower X-ray photon flux. The overall benefit of operating at lower laser energy can therefore be evaluated without compensating for the reduced photon flux through longer exposure times.

Figure 3 (g) displays the raw interferogram superimposed with the PMMA microspheres at laser energy E_2, with an exposure time t_1 averaged 4 times (configuration $[C]$) to match the total acquisition time of configuration $[A]$ (see Figure 3 (a)). The f-CNR value is 2.24 which is higher than the f-CNR value obtained for configuration $[A]$. Consistent with the previous observations, the h-SNR of the harmonic pair $H_{-1,1}$ and $H_{1,1}$ respectively reaches 20.72 and 20.48, remaining closer to the values obtained for configuration $[B]$ (h-SNR$_{E_2,\,t_2}$ $(H_{-1,1}, H_{1,1})$ $=$ $(20.71,\ 20.50)$) and significantly higher than for

configuration $[A]$ (h-SNR$_{E_1,t_1}(H_{-1,1}, H_{1,1}) = (13.69,\ 13.68)$). Contrary to conventional expectations based solely on photon statistics, the lower X-ray photon flux configuration yields phase images with a higher f-CNR. This counter intuitive result can be explained by considering the balance between photon flux and spatial coherence. While a higher flux reduces the statistical noise, the associated increase in focal spot size significantly degrades high-frequency content in the recorded interferogram. This leads to a reduction in fringe intensity contrast, which directly impacts the stability and robustness of the phase retrieval process. In contrast, the lower X-ray photon flux configuration preserves the high-frequency content of the interference pattern, resulting in improved fringe intensity contrast and more reliable phase demodulation as emphasised by the h-SNR values.

As reported in Table 2, the Pearson correlation scores ρ_x and ρ_y improve with respect to the configuration $[A]$, although they remain slightly below those obtained for the averaged configuration $[B]$, for which averaging over sixteen images further reduces the noise level. This behavior is also reflected in the Confidence Map, where the proportion of noise, undersampling and dislocation alerts, are consistently lower for the 4 mJ laser energy case compared to 12 mJ.

Conf.	Laser energy (mJ)	Acquisition time (s)	Pearson correlation coefficients ρ_x; ρ_y	Confidence Map values η_n ($\mu \pm \sigma$)	η_u^M ($\mu \pm \sigma$)	η_u^H ($\mu \pm \sigma$)
$[A]$	12	16×30	0.809; 0.806	0.150±0.128	0.016±0.036	0.006±0.056
$[B]$	4	16×120	0.881; 0.922	0.006±0.007	0.008±0.017	0.002±0.026
$[C]$	4	4×120	0.837; 0.882	0.012±0.013	0.013±0.029	0.004±0.041

Table 2. Phase retrieval quality criteria (Pearson correlation and Confidence Map) for the two laser energies considered for both cases: constant photon flux and constant acquisition time.

Discussion

The objective of this parametric study consisted to evaluate the influence of Kα laser–plasma X-ray source characteristics on MLSI performance, by distinguishing the respective contributions of photon statistics and source size to the quality of the retrieved phase images. Advantageously, working in the Fourier domain offers the key benefit of enabling a near-direct characterization of the emitting source geometrical properties, and in particular the anisotropy of its focal spot. The first-order harmonics arise from interferometric signal contributions associated with both the horizontal and vertical dimensions of the source, whereas the second-order harmonics encode information related solely to the spatial coherence along a single dimension (see details in Figure 5). Consequently, the harmonic signal-to-noise ratio (h-SNR) qualitatively assess about the 2D geometry of the emitting X-ray source volume. Thus, direct analysis of their h-SNR provides a first quantitative indication of the impact of the laser parameters choice. As expected, the h-SNR of all harmonics in the 12 mJ laser energy configuration are lower h-SNR compared to the 4 mJ laser energy configuration. In both cases, the diagonal harmonics ($H_{\pm1,\pm1}$) echibit a higher SNR in comparison with the horizontal and vertical ones ($H_{\pm2,0}$, $H_{0,\pm2}$), due to the frequency cutoff derived from geometric blur. At 12 mJ, both the f-SNR and the corresponding h-SNR are very low. Consequently, the h-SNR becomes less sensitive to the geometrical characteristics of the emitting source and no longer encodes meaningful information about its geometry. By comparison, at 4 mJ, the orthogonal harmonics ($H_{0\pm2}, H_{\pm2,0}$) exhibit higher h-SNR values along the vertical direction (19.44) than along the horizontal one (18.96) representing a discrepancy of 2.5 %, thereby allowing the source anisotropy to be identified.

In contrast to conventional absorption imaging, where increasing the number of detected photons directly improves the image signal-to-noise ratio, MLSI relies on the preservation of a periodic carrier signal generated by a checkerboard phase grating. Consequently, the phase retrieval performance depends not only on photon statistics but also on the ability of the imaging system to preserve the modulation of the carrier intensity fringes. Indeed, the iso-flux experiments demonstrate that photon statistics alone cannot explain the observed differences in phase image quality. By maintaining an equivalent number of detected photons while varying the laser energy, the influence of X-ray source characteristics (flux, size) was isolated. The degradation observed at higher laser energy is attributed to the broadening of the effective X-ray source, leading to a reduction of the transverse spatial coherence and consequently to a loss of high-frequency fringe modulation.

The fixed acquisition-time experiments further demonstrate that this conclusion remains valid under practical imaging conditions. When the total acquisition time is kept constant, a higher laser energy yields a higher detected photon flux but simultaneously enlarges the effective X-ray source size. Although the higher photon statistics are expected to improve the image quality, the associated loss of spatial coherence degrades the carrier fringe modulation and ultimately limits the phase retrieval performance. Under the investigated conditions, preserving the spatial coherence of the source therefore provides a greater benefit than increasing the photon flux alone. This behaviour is consistently reflected by all the evaluated image quality

metrics. The degradation of the interferograms is captured by both the f-CNR and h-SNR, while the reconstructed phase images exhibit lower Pearson correlation scores together with increased Confidence Map alerts.

Since the 4 mJ operating point provided the best compromise between photon flux and spatial coherence within the investigated laser conditions, it was interesting to further investigate the influence of acquisition averaging on the phase retrieval performance. As expected, progressively reducing the number of averaged acquisitions led to a degradation of all image quality metrics due to the greater contribution of the photon noise. Eventually, when photon statistics become too limited, the benefit provided by the spatial coherence is no longer sufficient to compensate for the increased statistical noise. For instance, with no averaging at 4 mJ with 120 s acquisition time the f-CNR is 1.32, the Pearson correlation scores are $\rho_x = 0.712$ and $\rho_y = 0.751$ and the Confidence Map alerts are, for the noise $\eta_n = 0.019 \pm 0.024$, and the undersampling alerts $\eta_u^M = 0.028 \pm 0.062$ and $\eta_u^H = 0.025 \pm 0.127$. Under these conditions, the higher photon flux obtained at 12 mJ becomes advantageous for the phase reconstruction. As such, a key outcome of this analysis is the identification of optimal operating conditions that balance three competing factors: photon statistics (noise level), spatial coherence (fringe contrast) and reconstruction stability.

Conclusion

This work demonstrates the feasibility of combining the MLSI technique with a laser-driven ultrafast hard Kα X-ray source for quantitative phase-contrast imaging. Beyond this proof of concept, it establishes a controlled experimental framework for evaluating MLSI performance under varying X-ray source operating conditions, allowing the respective influence of photon statistics and X-ray source size on phase retrieval quality to be quantitatively distinguished. Despite using a relatively low-sensitive X-ray detector at the Mo Kα energy (17.48 keV), accurate quantitative phase measurements of a millimetric test object were successfully achieved over a sub-centimeter field of view. Although the acquisition times remain prohibitively long for high-resolution phase-contrast imaging in the present laser-based X-ray platform, this study identifies the operating conditions that maximize MLSI performance and therefore provides practical guidelines for future implementation of the technique with compact laser-driven X-ray sources. The main limitation currently lies in simultaneously achieving high X-ray photon flux and high spatial coherence. More specifically, future developments may either increase the X-ray photon yield while operating at lower laser energies, where the X-ray source size remains minimal, or preserve a small source size while maintaining a high photon flux. These challenges are currently the focus of ongoing developments in laser-produced plasma technology. In particular, advances based on microstructured X-ray converter targets[41], higher repetition-rate laser systems[22,42], and longer-wavelength laser drivers[43] are expected to significantly improve source performance. Experimental hardware upgrades aiming at repetition rates approaching 1 kHz while preserving the current spectral and geometrical source characteristics are also investigated. Combining these technological advances with the framework developed in this study should allow quantitative phase-contrast imaging with improved temporal resolution and shorter acquisition time. In the same spirit, further improvements to the phase retrieval algorithm could first be achieved by suppressing the sample-only acquisition (see Methods). This could be accomplished using machine learning approaches, similar to those recently proposed for speckle-based X-ray imaging to mitigate the contribution of absorption[44]. In addition, the retrieved contrast modalities could be further enhanced by incorporating dark-field information, particularly for samples containing fine unresolved structures[45]. Finally, the applicability of other single-modulator phase-contrast imaging approaches and associated retrieval algorithms could be investigated in future work[46]. Such improvements would open the way toward compact laboratory implementations for applications including micro-computed tomography, time-resolved biological imaging[3], and materials science[4,5,47].

Methods

X-ray spectra

Prior to MLSI experiments, measurements based on well-tested procedure[33] have beeto characterize the X-ray source sizes (using knife edge technique[38]) and the emitted X-ray spectrum. Considering the spectrum, the direct-detection back-illuminated CCD camera (PIXIS-XB, Princeton Instruments) of 16-bits dynamic range is used as a dispersionless spectrometer operating in photon counting mode[48]. Photon counting mode consists in the detection of a single photon per pixel and per laser shot. In order to avoid pile-up problems due to the summation of the energy of more than one photon within one pixel, the number of laser shots (typically around tens of shots) is adjusted to get appropriate signal-to-noise ratio and accuracy in the investigated laser intensity regime. To reconstruct the emitted spectrum of the X-ray source, a home-developed software and a ^{57}Co radioactive calibration source allow us to obtain absolute X-ray spectra within the 2–30 keV photon energy range. For that, we take into account the quantum efficiency (including the Beryllium window placed in front of the detector), which depends on the photon energy, the transmission of the second Beryllium window located at the output of the vacuum chamber and the X-ray attenuation by the air from the output of the vacuum chamber, the solid angle of detection and the number of laser shots. Due to the limitations of our analysis procedure and of the spectral resolution of our detector, the precision of the spectrum reconstruction is $\sim$200 eV[49]. In this work, the reported number of emitted Kα photons is given within a spectral bandwidth of $\sim$1.7 keV. This

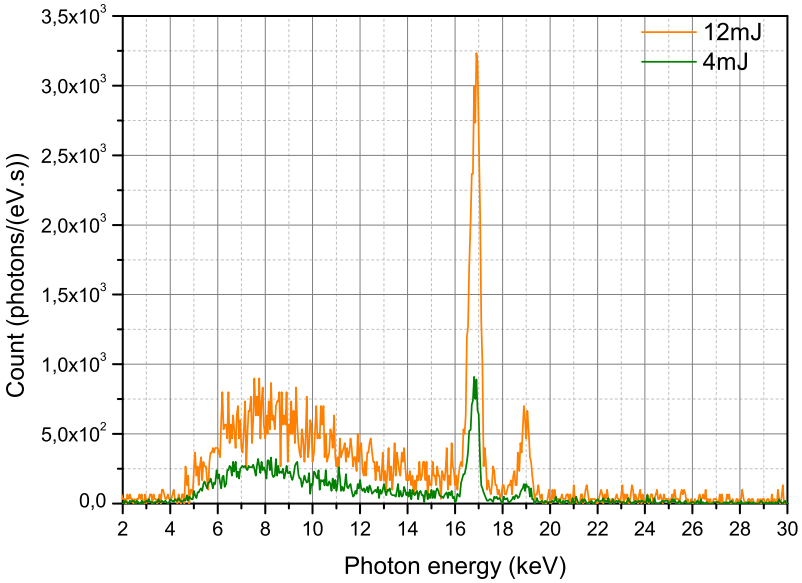

Figure 4. Reconstructed X-ray spectrum consistent with the PIXIS camera response, for two laser energies E_1(in orange) and E_2(in green). In this configuration, the sample and the grating are removed. The reconstructed spectrum takes into account the quantum efficiency of the detector and the spectral attenuation of the different absorbing elements. In particular, a Beryllium window (800-µm thick), sealing the interaction chamber attenuates the lower energies of the emitted X-ray spectrum ($\sim$ 15% of absorption at 8 keV). Below 4 keV, the spectrum is completely suppressed by the propagation through air. Note that the spectral sensitivity of the CCD detector strongly decreases below 2% at 30 keV (supplier data).

energy band covers the full extent of the Kα line bandwidth reconstructed by this procedure. In this case, the calculation takes into account the number of laser shots to determine an averaged Kα Mo spectrum. We further deduce the Kα photon number emitted by the source located in vacuum, here equal to $\sim$8 10^8 ph/sr/s for a laser energy of 4 mJ and $\sim$3.2 10^9 ph/sr/s for 12 mJ in our operating conditions at 100-Hz repetition rate.

This reconstructed emission spectrum slightly differs from the one shown in Figure 4 which presents the reconstructed X-ray spectrum detected by the PIXIS camera in the experimental configuration used for the MLSI acquisitions. Indeed, to assess the suitability of the MLSI imaging system applied to the Kα laser–plasma source, it is important to consider the X-ray spectrum involved in capturing the signal from the object under investigation and further in its detection by the CCD camera. Further, considering the spectral quantum efficiency of the CCD detector (manufacturer data), the Beryllium window transmission of the vacuum chamber and 75 cm propagation in air where the detector is located, the MLSI setup is sensitive to an X-ray flux ranging from $\sim$5 keV to $\sim$30 keV, with a detected photon transmission above $\sim$2% over this range. The level of transmission specific to Molybdenum Kα line is around 7%, mainly due to the low quantum efficiency of the detector at this energy. Low-energy radiation ($<$ 5 keV) following the Kα emission is filtered out by the beryllium window and air propagation, thereby minimizing interference noise associated with polychromatic illumination. As demonstrated in this article, although improvements are possible, in particular to reduce experimental acquisition time, this performance is sufficient to extract precise and quantitative information from a low-absorbing object. We can notice that over a spectral width close to $\sim$30 keV, around $\sim$20% detected photons specifically come from the Kα line for a laser energy of 4 mJ and is more monochromatic with a value close to $\sim$27% for a laser energy of 12 mJ. Made of thin squared gold platforms (1.7 µm thickness) on a polyimide substrate, the grating is designed to modulate the signal intensity particularly at the central wavelength of Kα line. Importantly, it does not reduce dramatically the available X-ray flux with an overall averaged transmission of $\sim$85% at $\sim$17.48 keV. In the Fourier domain, this translates into a high signal-to-noise ratio provided by the first harmonics. Because of the quantum efficiency of the detector, which peaks around $\sim$5-6 keV, a non-negligible amount of low-energy X-ray photons contribute to the MLSI signal by adding noise. This induces significant absorption signals that translate into the Fourier domain as a prominent central harmonic. As explained in the main article, this also impacts the phase gradient measurement, as the high spatial frequencies of the central harmonic signal are superimposed on the low-frequency signal of the higher harmonics. To overcome this, in real

space, the attenuation image of the sample is subtracted from the raw MLSI image, as detailed in the next sections. With this post-treatment strategy, the harmonics of first orders are not significantly altered by the high spatial frequencies from the central harmonic signal. The extraction of phase information provided by the first harmonics comes mainly from the contribution of monoenergetic Mo Kα photons.

Optimization of the experimental geometry

To perform accurate measurements, the experimental geometry of the X-ray phase-contrast imaging setup must satisfy several constraints related to fringe sampling, signal-to-noise ratio (SNR), and spectral bandwidth. The distance between the grating and the detector defines the grating magnification M_g, which determines the number of pixels of the detector illuminated and thus the sampling of the interferogram on the detector. The number of detector pixels corresponding to one period of the interferogram is given by $N = aM_g/S_{pix}$, where a is the grating period and a_{pix} the detector pixel size. To accurately sample the fringe modulation, at least six pixels per period are required. Increasing the grating-to-detector distance improves the sampling but simultaneously degrades the contrat-to-noise ratio as a decreasing period of the interferogram becomes more sensitive to geometric blur. The grating period therefore constitutes an additional parameter to carefully handle, as it directly influences both the phase sampling conditions and fringe intensity contrast.

In addition to these geometrical considerations, the residual spectral bandwidth of the femtosecond Kα source must also be taken into account. Although these sources are largely monochromatic with a prominent Kα line over a wide Bremsstrahlung background emission, the MLSI technique can be performed with polychromatic illumination provided that the detector is positioned beyond the achromatic distance. Beyond this distance, the interferogram generated by the phase grating becomes insensitive to the spectral distribution of the source.

For a plane-parallel incident beam, the achromatic distance $d_{\mathrm{ach,p}}$ is determined by the grating period a and the considered spectral bandwidth $\Delta\lambda$ according to[30]:

$$d_{\mathrm{ach,p}} = \frac{a^2}{\Delta\lambda}. \tag{1}$$

For the cone-beam geometry produced by the laser–plasma X-ray source, the achromatic distance $d_{\mathrm{ach,c}}$ is obtained when the chromatic shift of the interference pattern equals one apparent grating period. The latter is magnified by the beam divergence and is given by $a\left((d_{\mathrm{ach,c}} + d_{gs})/d_{gs}\right)$, while the chromatic shift is $(\Delta\lambda/a)\, d_{\mathrm{ach,c}}$. Using the sign convention of geometrical optics, where $d_{gs} = -d_{sg}$, this condition can be written as:

$$\frac{\Delta\lambda}{a} d_{\mathrm{ach,c}} = a\left(\frac{d_{gs} + d_{\mathrm{ach,c}}}{d_{gs}}\right). \tag{2}$$

Using Eq. (1) and Eq. (2), the achromatic distance for the cone-beam configuration can be expressed as:

$$\frac{1}{d_{\mathrm{ach,c}}} = \frac{1}{d_{\mathrm{ach,p}}} - \frac{1}{d_{gs}}. \tag{3}$$

For a grating period of $a = 36$ µm and a spectral bandwidth $\Delta E = 1.7$ keV (corresponding to the width of the Mo Kα line reconstructed from the measured spectrum shown in Figure 4), the achromatic distance is $d_{\mathrm{ach,p}} = 1.78$ m for a plane-parallel beam and $d_{\mathrm{ach,c}} = 20$ cm in the cone-beam configuration. The calculation above assumes that the Mo Kα emission provides the dominant contribution to the detected signal. Considering the entire detected spectral range ($\Delta E = 25$ keV) changes the cone-beam achromatic distance only marginally, as summarized in Table 3. Taking all these constraints into account, the source-to-grating (d_{sg}), source-to-sample (d_{so}), and source-to-detector (d_{tot}) positions have been selected to provide a grating magnification of $M_g = 4.2$, a sample magnification of $M_s = 3.6$, and a sampling of $N = 11.6$ pixels per fringe. The selected grating-to-detector distance also exceeds the calculated achromatic distance, ensuring adequate fringe sampling and wavelength-independent interferogram formation while maintaining a compact experimental setup.

	$\Delta E = 1.7$ keV	$\Delta E = 25$ keV
$d_{\mathrm{ach,p}}$ (m)	1.78	26.13
$d_{\mathrm{ach,c}}$ (m)	0.20	0.22

Table 3. Achromatic distance as a function of the spectral bandwidth considered in the calculation.

Phase retrieval and image acquisition procedure

Figure 5 presents the general pipeline of the phase image retrieval process and the quantitative analysis used in this study. MLSI is based on a checkerboard grating introducing X-ray tilted replicas that further interfere resulting in a regularly distributed pattern of maxima and minima in the intensity image recorded by the CCD camera, called a raw interferogram (see Figure 5 (a)). The phase and amplitude variations induced by the sample are compared to a reference interferogram acquired without the sample. Due to the regular periodicity of the grating, these variations can be extracted by working in the Fourier space. Indeed, the intensity modulation pattern is composed of several sinusoidal functions with distinct spatial frequencies (see Figure 5 (b)), each carrying wavefront information along a given spatial direction. The harmonics $H_{\pm1,\pm1}$ and $H_{0\pm2,0\pm2}$ carry the phase-gradient information. In this work, the measured phase gradients along the two diagonal directions are obtained from the harmonic pair $H_{1,1}$ and $H_{1,-1}$ (Figure 5 (c)). The phase gradients are retrieved from the argument of the inverse Fourier transform of each selected harmonic after applying an extraction window centered on the corresponding carrier frequency[50] (see yellow square in Figure 5 (b)). In principle, eight phase-gradient images can be extracted. The size of the extraction window is limited by the distance between two consecutive harmonics in the Fourier plane. Finally, using two orthogonal phase-gradient images (Figure 5 (c)), the Fourier derivative theorem[51] is applied to retrieve the phase image (Figure 5 (f)). Note that the central harmonic $H_{0,0}$ contains both the attenuation and the phase curvature intensity (highlighted by intensity overshoots on the edges of the PMMA microspheres). In practice, the finite extent of the harmonic peaks in Fourier space leads to partial overlap

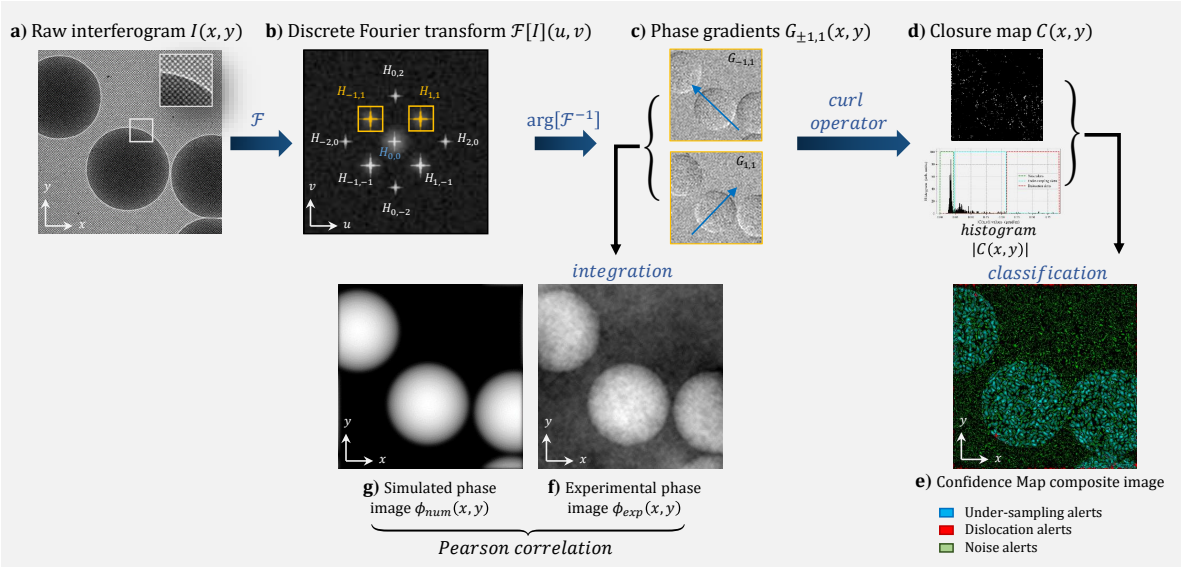

Figure 5. Phase extraction process, phase quality assessment using Pearson correlation, and self-assessment of error based on the Confidence Map.

between neighbouring harmonics. This is especially true with the central harmonic $H_{0,0}$ which may introduce artefacts in the retrieved phase image. Therefore, a correction method[52] is applied, which consists of subtracting the attenuation contribution and phase curvature of the sample with optimized weighting coefficients prior to Fourier analysis, thereby minimizing the contribution of $H_{0,0}$ to the other harmonics. For this purpose, three successive experimental configurations are required to retrieve the phase image: (i) sample alone, (ii) sample and grating, and (iii) grating alone. Besides reducing harmonic crosstalk, this acquisition strategy allows us to (i) image the sample in free-propagation mode together with its absorption contribution, (ii) retrieve the phase shift induced by the sample, and (iii) obtain a reference interferogram. Experimentally, the exposure time of each individual acquisition (t_1 or t_2, depending on the selected laser energy) was chosen to maximize the recorded signal while keeping the same 16-bits dynamic range of the X-ray CCD camera.

Raw data analysis

The performance of the imaging system can be first evaluated on the raw data (see Figure 5 (a,b)). The quality of the intensity modulation fringes has a direct impact on the accuracy of the phase-gradient measurement. To quantify both the fringe contrast and the robustness of the fringe pattern against noise, the intensity modulation along a direction perpendicular to the fringes was fitted with a sinusoidal function $I(x) = I_0 + A\cos[(2\pi x/a) + \phi]$ where I_0 is the mean intensity, A is the modulation amplitude and ϕ is the phase offset. The quality of the fringe pattern was quantified using the fringe contrast-to-noise ratio (f-CNR), defined as $\mathrm{f-CNR} = A/\sigma_{\mathrm{res}}$ where σ_{res} corresponds to the standard deviation of the difference between the measured intensity

and the fitted sinusoidal profile. This parameter accounts simultaneously for the fringe modulation amplitude and the deviation of the experimental profile from the ideal sinusoidal model, providing a quantitative measure of the effective fringe quality for phase-gradient retrieval.

From the discrete Fourier transform of raw datas, the harmonics signal to noise ratio (h-SNR) can be evaluated as well. For that we define ROI $\Omega_{(i,j)}$ centered on the harmonics $H_{\pm1,\pm1}$, $H_{0\pm2,0\pm2}$ and $H_{0,0}$ with the diagonal size defined as the distance between the central harmonic and $H_{\pm1,\pm1}$. An example of ROI (yellow square) is shown on the Figure 6 (a) for $H_{1,\pm1}$. For each harmonics in $\Omega_{(i,j)}$ the maximum pixel value H_{max} is recorded (see for example the case of $H_{1,1}$ in Figure 6 (a)). Then the maximum entropy threshold method[53] is applied (Figure6 (b)) to remove the harmonics peak contribution in $\Omega_{(i,j)}$ in order to estimate the noise σ_N by calculating the average values of the remaining pixel. In essence, this method aims to find the threshold Th that best distinguishes between different regions in the image, here the harmonic peak amplitude, by maximizing the overall uncertainty or disorder in the histogram distribution. Then the h-SNR can be estimated, defined as $\text{h}-\text{SNR} = 10(H_{max}/\sigma_N)$.

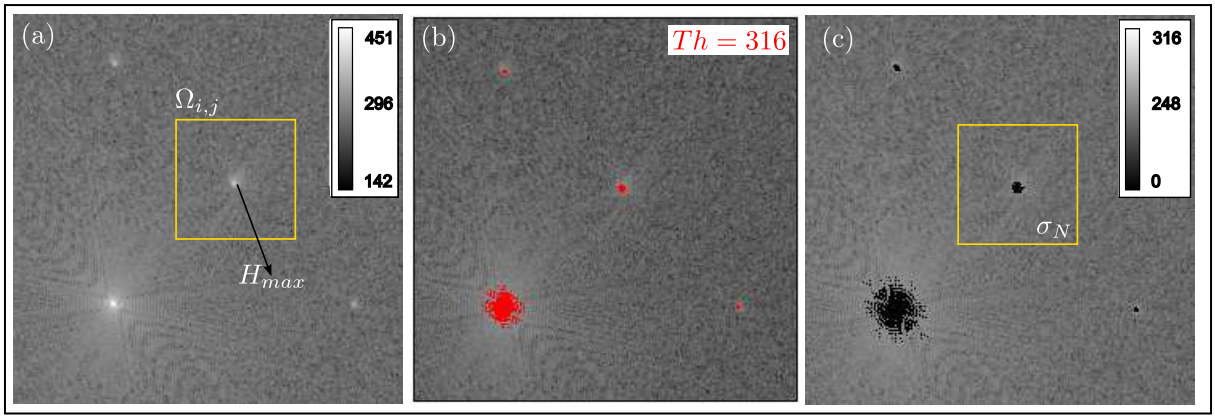

Figure 6. Description of the h-SNR calculation. A zoom on the up right quarter of the FFT was chosen to highlight the method. (a) Definition of the ROI $\Omega_{i,j}$ centered on a harmonic ($H_{1,1}$ here). Measurement of the maximum pixel value H_{max}. (b) Use of the maximum entropy threshold method to subtract the highest pixel values (red signal) related to the harmonics. (c) Calculation of the average value of the remaining pixels set as noise σ_N.

Pearson correlation

To quantitatively assess deviations of the experimental phase images from the idealized reference, the agreement between the experimental and simulated data is evaluated using Pearson correlation coefficients. Pearson correlation is employed because it quantifies the strength of the linear relationship between two datasets. Although it is defined for univariate signals, this assumption is appropriate in the present case, as the experimental and reference phase values are compared line by line and column by column. The mean Pearson correlation coefficients, (ρ_x) and (ρ_y), are calculated along the x and y-directions by evaluating the correlation for each image row x_i and column y_j, respectively:

$$\rho_{x_i} = \frac{\text{cov}(\phi, \phi_{ref})}{\sigma_\phi \ \sigma_{\phi_{ref}}}(x_i, y) \ , \ \rho_x = \underset{i\in\{1,\dots,n\}}{\text{mean}} \left[\rho_{x_i}\right], \tag{4a}$$

$$\rho_{y_j} = \frac{\text{cov}(\phi, \phi_{ref})}{\sigma_\phi \ \sigma_{\phi_{ref}}}(x, y_i) \ , \ \rho_y = \underset{j\in\{1,\dots,n\}}{\text{mean}} \left[\rho_{y_j}\right], \tag{4b}$$

where cov refers to the covariance function and $\sigma_\phi, \sigma_{\phi_{ref}}$ measure respectively the dispersion of the values in ϕ and ϕ_{ref} at the line x_i or the column y_j. Finally, n is the length of each axis.

Confidence Map

By performing the Confidence Map[34,35], an estimation of the experimental errors associated with the retrieved phase image can be obtained. Taking advantage of MLSI to measure at least two orthogonal phase gradients simultaneously, a phase-derivative closure map (see Figure 5 (d)) is calculated by applying the curl operator to the measured gradient field. For a continuous wavefront that is twice differentiable, the curl of the phase gradient is theoretically zero everywhere. Consequently, any non-zero closure value reveals inconsistencies between the measured gradients. These deviations originate from experimental limitations such as measurement noise, insufficient spatial sampling, or demodulation errors[34] (see Figure 5 (e)). The Confidence Map exploits the statistical distribution of the closure values to identify the physical origin of these deviations. A generalized

Gaussian mixture model is used to assign each pixel to either the noise contribution (η_n) or the undersampling contribution (η_u) according to its closure magnitude[35]. The resulting probabilistic classification is then spatially regularized to obtain coherent error maps. undersampling is further separated into two operational classes. High-magnitude undersampling (η_u^H) corresponds to the strongly nonlinear demodulation regime encountered near the sampling limit and is characterized by narrow, high-amplitude closure residuals localized along sharp interfaces. Medium-magnitude undersampling (η_u^M) comprises broader residuals of moderate amplitude that occur both within textured regions and in the vicinity of object boundaries.

Funding

This work is part of the ULTRAFAST project of PEPR LUMA and has benefited from State aid managed by the National Research Agency under France 2030 bearing the reference ANR-22-EXLU-0002. Ministry of Research and High Education, Region Provence-Alpes-Côte d'Azur, Department of Bouches-du-Rhône, City of Marseille, CNRS, and Aix-Marseille University are acknowledged for funding ASUR platform. The project leading to this publication has received funding from Excellence Initiative of Aix-Marseille University - A*MIDEX, a French "Investissements d'Avenir" program (AMX-19-IET-002).

Data availability

The data presented in this study are available from the corresponding authors on reasonable request.

Author contributions

Amélie Ferré and Adrien Stolidi conceived the study. Georges Giakoumakis, Amélie Ferré, Raphaël Clady and Adrien Stolidi conducted the experiment. Georges Giakoumakis, Amélie Ferré, Daria Gudz, Mouad Saliji and Adrien Stolidi analysed the results. Georges Giakoumakis, Amélie Ferré and Adrien Stolidi wrote the paper. All authors reviewed the manuscript.

References

1. Momose, A. X-ray phase imaging reaching clinical uses. *Phys. Medica* **79**, 93–102 (2020).
2. Bennett, E. E., Kopace, R., Stein, A. F. & Wen, H. A grating-based single-shot X-ray phase contrast and diffraction method for in vivo imaging. *Med. Phys.* **37**, 6047–6054 (2010).
3. Shaker, K., Häggmark, I., Reichmann, J., Arsenian-Henriksson, M. & Hertz, H. M. Phase-contrast X-ray tomography resolves the terminal bronchioles in free-breathing mice. *Commun. Phys.* **4**, 259 (2021).
4. Gruse, J.-N. *et al.* Application of compact laser-driven accelerator X-ray sources for industrial imaging. *Nucl. Instruments Methods Phys. Res. Sect. A: Accel. Spectrometers, Detect. Assoc. Equip.* **983**, 164369 (2020).
5. Massimi, L. *et al.* Time resolved in-situ multi-contrast X-ray imaging of melting in metals. *Sci. Reports* **12**, 12136 (2022).
6. Guitard, L. *et al.* Robust quantitative X-ray phase diagnostic for carbon composite characterisation in the context of lightning induced risk. *Sci. Reports* **14**, 21803 (2024).
7. Weitkamp, T. *et al.* X-ray phase imaging with a grating interferometer. *Opt. express* **13**, 6296–6304 (2005).
8. Antonelli, L. *et al.* X-ray phase-contrast imaging for laser-induced shock waves. *EuroPhysics Lett.* **125**, 35002 (2019).
9. Quenot, L., Bohic, S. & Brun, E. X-ray phase contrast imaging from synchrotron to conventional sources: A review of the existing techniques for biological applications. *Appl. Sci.* **12**, 9539 (2022).
10. Wilkins, S., Gureyev, T. E., Gao, D., Pogany, A. & Stevenson, A. Phase-contrast imaging using polychromatic hard X-rays. *Nature* **384**, 335–338 (1996).
11. Leatham, T. A., Paganin, D. M. & Morgan, K. S. X-ray phase and dark-field computed tomography without optical elements. *Opt. Express* **32**, 4588–4602 (2024).
12. Takeda, Y. *et al.* X-ray phase imaging with single phase grating. *Jpn. journal applied physics* **46**, L89 (2007).
13. Morgan, K. S., Paganin, D. M. & Siu, K. K. Quantitative single-exposure x-ray phase contrast imaging using a single attenuation grid. *Opt. express* **19**, 19781–19789 (2011).
14. Olivo, A. Edge-illumination x-ray phase-contrast imaging. *J. Physics: Condens. Matter* **33**, 363002 (2021).
15. Pfeiffer, F., Weitkamp, T., Bunk, O. & David, C. Phase retrieval and differential phase-contrast imaging with low-brilliance X-ray sources. *Nat. Phys.* **2**, 258–261 (2006).

16. Zanette, I. *et al.* Speckle-based X-ray phase-contrast and dark-field imaging with a laboratory source. *Phys. Rev. Lett.* **112**, 253903 (2014).

17. Snigirev, A., Snigireva, I., Kohn, V., Kuznetsov, S. & Schelokov, I. On the possibilities of X-ray phase contrast microimaging by coherent high-energy synchrotron radiation. *Rev. Sci. Instruments* **66**, 5486–5492 (1995).

18. Park, H.-S. *et al.* High-resolution 17–75keV backlighters for high energy density experiments. *Phys. Plasmas* **15** (2008).

19. Joshi, C., Corde, S. & Mori, W. B. Perspectives on the generation of electron beams from plasma-based accelerators and their near and long term applications. *Phys. Plasmas* **27**, 070602 (2020).

20. Nejdl, J. *et al.* Update on laser-driven x-ray sources at eli beamlines. In *Compact EUV & X-ray Light Sources*, ETh5A–6 (Optica Publishing Group, 2022).

21. Azamoum, Y. *et al.* High photon flux Kα Mo X-ray source driven by a multi-terawatt femtosecond laser at 100 Hz. *Opt. Lett.* **43**, 3574–3577 (2018).

22. Koç, A. *et al.* Compact high-flux hard X-ray source driven by femtosecond mid-infrared pulses at a 1 kHz repetition rate. *Opt. Lett.* **46**, 210–213 (2021).

23. Toth, R., Kieffer, J. C., Fourmaux, S., Ozaki, T. & Krol, A. In-line phase-contrast imaging with a laser-based hard X-ray source. *Rev. Sci. Instruments* **76**, 083701 (2005).

24. Burvall, A., Lundström, U., Takman, P. A., Larsson, D. H. & Hertz, H. M. Phase retrieval in X-ray phase-contrast imaging suitable for tomography. *Opt. Express* **19**, 10359–10376 (2011).

25. Alloo, S. J. *et al.* Tomographic phase and attenuation extraction for a sample composed of unknown materials using X-ray propagation-based phase-contrast imaging. *Opt. Lett.* **47**, 1945–1948 (2022).

26. Yang, X. *et al.* Self-supervised physics-informed generative networks for phase retrieval from a single x-ray hologram. *Opt. Express* **33**, 35832–35851 (2025).

27. Bouffetier, V. *et al.* Proof-of-concept Talbot–Lau X-ray interferometry with a high-intensity, high-repetition-rate, laser-driven Kα source. *Appl. Opt.* **59**, 8380–8387 (2020).

28. Ivanov, K., Gavrilin, I., Volkov, R., Gavrilov, S. & Savel'Ev, A. Thicket high Z wavelength-scale structured target: advantages and limitations for laser-driven hard X-ray source and phase contrast imaging. *Laser Phys. Lett.* **18**, 075401 (2021).

29. Primot, J. Three-wave lateral shearing interferometer. *Appl. Opt.* **32**, 6242–6249 (1993).

30. Rizzi, J. *et al.* Quadriwave lateral shearing interferometry in an achromatic and continuously self-imaging regime for future X-ray phase imaging. *Opt. letters* **36**, 1398–1400 (2011).

31. Utéza, O. *et al.* High flux sub-picosecond laser-based hard x-ray platform for advanced material analysis and imaging. *Rev. Sci. Instruments* **97**, 013006 (2026).

32. Gambari, M. *et al.* Exploring phase contrast imaging with a laser-based Kα X-ray source up to relativistic laser intensity. *Sci. Reports* **10**, 6766 (2020).

33. Azamoum, Y. *et al.* Impact of the pulse contrast ratio on molybdenum Kα generation by ultrahigh intensity femtosecond laser solid interaction. *Sci. Reports* **8**, 4119 (2018).

34. Stolidi, A., Giakoumakis, G., Primot, J., Jarnac, A. & Tisseur, D. Confidence map tool for gradient-based x-ray phase contrast imaging. *Opt. Express* **30**, 4302–4311 (2022).

35. Saliji, M., Stolidi, A., Primot, J. & Jarnac, A. Confidence map for multi-gradient-based x-ray phase-contrast imaging: a probabilistic error classification approach. *Opt. Lett.* **51**, 1959–1962 (2026).

36. Henke, B. L., Gullikson, E. M. & Davis, J. C. X-ray interactions: photoabsorption, scattering, transmission, and reflection at E= 50-30,000 eV, Z= 1-92. *At. Data Nucl. Data Tables* **54**, 181–342 (1993).

37. Gambari, M. *et al.* Experimental investigation of size broadening of a Kα X-ray source produced by high intensity laser pulses. *Sci. Reports* **11**, 23318 (2021).

38. Alaterre, P., Popovics, C., Geindre, J. P. & Gauthier, J. C. A study of the spectral emissions in laser-irradiated microdot targets at 0.53 and 0.27 μm wavelengths with micron resolution. *Opt. Commun.* **49**, 140–145 (1984).

39. Boschetto, D. *et al.* Spatial coherence properties of a compact and ultrafast laser-produced plasma keV X-ray source. *Appl. Phys. Lett.* **90** (2007).

40. Chen, L. *et al.* Study of X-ray emission enhancement via a high-contrast femtosecond laser interacting with a solid foil. *Phys. Rev. Lett.* **100**, 045004 (2008).

41. Samsonova, Z. *et al.* Hard X-ray generation from ZnO nanowire targets in a non-relativistic regime of laser-solid interactions. *Appl. Sci.* **8**, 1728 (2018).

42. Rimkus, L. *et al.* Compact high-flux X-ray source based on irradiation of solid targets by gigahertz and megahertz bursts of femtosecond laser pulses. *Opt. Continuum* **1**, 1819–1836 (2022).

43. Barbrel, B. *et al.* Demonstration of a robust laser-driven X-ray source for CT. In *Proceedings of 13th Conference on Industrial Computed Tomography, Wels, Austria*, 29,1 (2024).

44. Yu, F. *et al.* Dynamic x-ray speckle-tracking imaging with high-accuracy phase retrieval based on deep learning. *IUCrJ* **11**, 73–81 (2024).

45. Wen, H. H., Bennett, E. E., Kopace, R., Stein, A. F. & Pai, V. Single-shot x-ray differential phase-contrast and diffraction imaging using two-dimensional transmission gratings. *Opt. letters* **35**, 1932–1934 (2010).

46. Kefs, S. *et al.* Universal and quantitative statistical approach to retrieve x-ray directional dark-field using a single exposure. *Opt. Open* (2025).

47. Garcea, S. C., Wang, Y. & Withers, P. J. X-ray computed tomography of polymer composites. *Compos. Sci. Technol.* **156**, 305–319 (2018).

48. Fourment, C. *et al.* Broadband, high dynamics and high resolution charge coupled device-based spectrometer in dynamic mode for multi-keV repetitive X-ray sources. *Rev. Sci. Instruments* **80**, 083505 (2009).

49. Azamoum, Y. *Etude du rayonnement X Kα du molybdène issu de l'interaction laser solide à fort contraste temporel*. Ph.D. thesis, Aix-Marseille Université (2016).

50. Takeda, M., Ina, H. & Kobayashi, S. Fourier-transform method of fringe-pattern analysis for computer-based topography and interferometry. *J. Opt. Soc. Am.* **72**, 156–160 (1982).

51. Paganin, D. *Coherent X-Ray Optics* (Oxford University Press, United Kingdom, 2006), 1 edn.

52. Giakoumakis, G., Primot, J., Jarnac, A., Guitard, L. & Stolidi, A. Artifacts reduction in high-acutance phase images for X-ray grating interferometry. *Opt. Express* **30**, 41147–41156 (2022).

53. Kapur, J. N., Sahoo, P. K. & Wong, A. K. A new method for gray-level picture thresholding using the entropy of the histogram. *Comput. vision, graphics, image processing* **29**, 273–285 (1985).